Journal of the European Ceramic Society 42 (2022) 193–201

Contents lists available at ScienceDirect

Journal of the European Ceramic Society

journal homepage: www.elsevier.com/locate/jeurceramsoc

Influences of the solid load on the microstructure and compressive behavior of Fe_2O_3 scaffolds manufactured by freeze-casting using stearic acid as dispersant agent

P.J. Lloreda-Jurado [a], Victor Perez-Puyana [b], Alberto Romero [b], R. Sepúlveda [a,*]

[a] Ingeniería y Ciencia de los Materiales y del Transporte, E.T.S. de Ingeniería, Universidad de Sevilla, Avda. Camino de los Descubrimientos s/n., 41092, Sevilla, Spain
[b] Departamento de Ingeniería Química, Facultad de Química, Universidad de Sevilla, 41012, Sevilla, Spain

ARTICLE INFO

Keywords:
Camphene
Stearic acid
Freeze-casting
Rheology
Compression strength

ABSTRACT

Porous materials manufactured by freeze-casting are demonstrating potential application as oxygen carriers for the production and purification of hydrogen, or anode material for lithium-ion batteries. However, to obtain the required pore morphology and sufficient mechanical strength, the suspension processing parameters must be controlled. Fe_2O_3 nanoparticles/camphene suspensions were fabricated using stearic acid as the dispersant agent showing a low-viscosity (130 mPa·s) with a high solid volume fraction (0.3). Suspensions show a shear-thinning behavior according to the Sisko model and a maximum packing fraction of 0.569 estimated from a zero porosity sample. A modified Krieger and Dougherty model was introduced to incorporate the influence of the particle-aspect ratio. The Fe_2O_3 scaffolds manufactured by freeze-casting shown a gradient pore size along the freezing direction, which was diminished with the solid volume fraction, the compression strength was improved with the pore size reduction and fitted according to the minimum solid area model.

1. Introduction

The interest in the freeze-casting technique has grown over the last 20 years due to its ability to build porous materials with a wide diversity of raw powders [1–4]. The potential of this technique lies in the possibility of tailoring the pore morphology by controlling the parameters of the manufacturing process, especially those related to the cooling and solidification of the liquid vehicle. The freeze-casting technique begins with the formation of a stable particle suspension, which later solidifies directionally to allow dendrites to grow. Dendrites push the suspended particles and stack them into interdendritic spaces; the solid solvent is then removed by sublimation and the green samples are finally sintered. Ceramic materials have been the leading choice [5–9] for decades due to their chemical variety and abundance in the submicrometric range. However, metals [10,11], plastics [12], and metallic oxides [13,14] are now being extensively employed to create porous materials. Today, Fe_2O_3 particles [15,16] or scaffolds [13,17,18] are drawing major attention due to their redox properties, which constitute a feasible and valid alternative for the production, storage, and purification of hydrogen. However, the operational temperature of the redox cycles promotes particle sintering and the reduction of open porosity, which cause a significant drop in performance efficiency due to the diminishing of accessible reactive surfaces. A simple solution is to dope the metal oxide to add elements such as Al, Mg, Zr, or Ce [15] and increase the open porosity to counterbalance the sintering process. In the case of the freeze-casting technique, open porosity could be increased by controlling the solidification process, reducing the powder load in the initial slurry, and decreasing the effective particle size to allow dendrite replication and proper stacking during solidification.

Although water has been the main solvent used for obvious reasons, camphene is also employed as a liquid vehicle to fabricate porous materials [19]. Camphene ($C_{10}H_{16}$) is a non-polar organic component of the terpene family, with a melting point of 48−51 °C [20,21], an ability to form branched dendrites during solidification, and it sublimates under ambient conditions. Due to the non-polar characteristic of camphene, the numbers of suitable additives are limited. Polystyrene (PS) has proved to be a suitable binder [22], while fatty acid polymer [23] and, the most common, polyester oligomer [24,25] (i.e., Hypermer KD4®, Zephrym®, Solsperse 3000®, etc.) are the main choices as dispersant agents. Polyester oligomer has been used to create zirconia suspensions in non-polar [26] and organic media [27]. According to Moloney et al. [26], polyester oligomer employs its carboxyl functional group as a

* Corresponding author.
E-mail address: rsepulveda@us.es (R. Sepúlveda).

https://doi.org/10.1016/j.jeurceramsoc.2021.09.056
Received 16 June 2021; Received in revised form 9 September 2021; Accepted 26 September 2021
Available online 28 September 2021

particle anchor. This functional group allows the formation of chelate complexes around the particle surfaces by keeping it strongly adsorbed to the particle while the other side of the molecule shows good affinity with the solvent. Thus, the 90-carbon chain molecule forms a steric barrier (10 nm in length) that reduces the particle attraction forces, thereby creating a more stable suspension. In the case of metal oxide nanoparticles with a typical range size of 10−50 nm, this dispersant may form a heavy and thick stearic barrier that could lead to unwanted effects during freeze-cast processing, such as: particle precipitation, inefficient particle stacking, and excessive viscosity at high particle loading. Therefore, the use of a carboxylic acid with a lower hydrocarbon chain, such as stearic acid, could improve the handling of slurries with high solid loading and improve the mechanical properties of the metal oxide scaffolds created by freeze-casting.

This work is focused on the use of stearic acid (SA) as a particle dispersant and its effects on the pore structure and mechanical performances of Fe_2O_3 scaffolds. The SA is a carboxylic acid with an 18-carbon chain molecule and produce a steric barrier length of just 4 nm [27], which appears sufficient for nanoparticle to achieve a complete stearic stabilization, to improve the particle staking during solidification, and, lastly, to enhance the mechanical properties. The viscosity of camphene suspensions has been characterized as a function of the solid volume fraction. These suspensions have been employed to manufacture hematite scaffolds with gradient porosity by freeze-casting, the size and morphology of which have been characterized by optical microscopy and scanning electron microscopy (SEM). This study was completed with the mechanical characterization of the material through the responses to compression loads.

2. Experiment and method

2.1. Scaffold manufacturing

Fe_2O_3 nanoparticles/camphene suspensions with 10, 20 and 30 vol. % of solid load, i.e. a solid volume fraction $\phi = 0.1$, 0.2, and 0.3, were made by ball-milling at 60 °C. The nanoparticle α-Fe_2O_3 powder (99.8 %, GNM, Saint-Cannat, France) employed has a rod-like shape with a particle size of 30 nm in length by 8 nm in diameter, confirmed by transmission electron microscopy observation (TEM), and has a specific surface area of 101 m^2/g determined by BET (Brunauer, Emmett and Teller) theory. Camphene (95 %, Sigma Aldrich, Madrid, Spain) was used as liquid media. An 8 wt.% of stearic acid (SA) (98 %, Alfa Aesar, Barcelona, Spain) according to the powder load was added as the dispersant agent. The scaffold manufacturing procedure was based on a previous study [13]. Firstly, the dispersant agent was mixed for 30 min in camphene and the powder was subsequently added to the media and ball-milled for a further 24 h to achieve proper particle dispersion.

Before pouring, the suspensions were sonicated for 10 min to remove any air bubbles formed during the ball-milling process. The degassed suspension was then poured into a cylindrical mold of 30 mm in diameter by 15 mm in height made of PTFE walls and a copper base, which was pre-heated at 60 °C in an incubator. The poured suspension was prerested for 15 min before any cooling was applied. The directional cooling was performed by running water at 42.5 °C across the mold base and gradually reducing the incubator temperature at a rate of 0.2 °C·min^{-1} until complete sample solidification was attained.

Once the samples reached complete solidification, they were kept at room temperature for 48 h to allow the solid camphene to sublimate. Finally, the green samples were heat-treated in a tubular furnace (Tube furnace Thermolyne 21100, Merck, Germany) at 600 °C for 2 h for organic burn-out and sintered at 1100 °C for 3 h. All heat treatments were carried out in an air atmosphere. The heating and cooling rates were set at 1 °C·min^{-1} and 5 °C·min^{-1}, respectively, to prevent cracks or sample distortions. The sintered samples were approximately 9 mm in height by 20 mm in diameter.

2.2. Rheological characterization

Rheological characterization was conducted using a stress-controlled rheometer (AR2000, TA Instruments). Steady-state flow curves were obtained for each suspension immediately after being ball-milled for 24 h and shear viscosity values were recorded from 1 to 100 s^{-1}. Experiments were performed using a 50 mm-diameter parallel-plate geometry, with a 500 μm gap between plates. The temperature was fixed at 60 °C for all experiments using a Peltier system accessory. Additionally, 4 suspensions with $\phi = 0.1$ were prepared with different concentrations of SA (1, 2, 4, and 8 wt.%) to determine the point of minimal viscosity measured at 100 s^{-1}.

2.3. Scaffold microstructure characterization

The pore structure of the sintered hematite scaffolds was analyzed with Field Emission Scanning Electron Microscopy (FESEM) and Optical Microscopy (OM). Several images of the central axial plane were taken at different heights ($h = 0$, 3, 6, 9 mm) to quantify the average pore and wall sizes using the non-redundant maximum-sphere-fitted image analysis technique [28]. An area of approximately 1 mm^2 was analyzed at each h. Pore size distributions were measured by Quantachrome Poremaster 60GT mercury porosimeter using a sample of 3 × 3 mm in area by 9 mm in height (the longest axis was parallel to the freezing direction). Total porosity (%) was determined by three procedures: a) Archimedes' method: soaking the sintered samples into boiling water for 5 h and leaving them immersed in the hot water for a further 24 h; b) Mercury Intrusion Porosimetry using a Quantachrome Poremaster 60GT porosimeter; and c) Image analysis: the free access ImageJ software was used for image processing (8-bit binarization, threshold, and removal of 4-pixel outliers).

2.4. Mechanical characterization

Compression tests were carried out at room temperature using an Instron 5505 with a 100 N load cell and a cross-head speed of 2 mm·min^{-1}. The tests were performed over cubes with 4 mm in length which were cut from the sintered samples of the top ($h = 9$ mm) and bottom ($h = 0$ mm) sections. Loading directions were applied either parallel or perpendicular to the solidification direction, 3 samples were tested on each condition. All tests were halted when a decrease of over 30 % on the applied stress was detected. The results showed the mean of these replicates and uncertainty was expressed in terms of SD (standard deviation) using Excel from the Microsoft Office 2019 statistical package.

3. Results and discussion

3.1. Rheology of nanoparticle suspensions

The steady-state flow curves obtained as a function of the solid volume fraction (Fig. 1) showed an increase in the measured viscosity with the powder loading, as was expected [19,29]. The use of SA as a dispersant agent produced slurries with sufficiently low viscosity to pour without difficulty, where the viscosity of the molten camphene at 60 °C is 1.60 mPa·s [30]. The curves showed a reduction in the measured viscosity (η) as the shear rate ($\dot{\gamma}$) increased. At low $\dot{\gamma}$, no constant values of the viscosity (η_o) were determined, but at approximately 100 s^{-1} the measured viscosity (η_{100}) achieved nearly a constant value, which increased with the solid volume fraction (ϕ) in the slurries. The viscosity curves were strongly dependent on the shear stress, as the measured η decreases with the $\dot{\gamma}$ (Fig. 1). The slurries with a solid volume fraction of $\phi = 0.2$ and 0.3 were close to each other and showed a significant drop in viscosity as the shear rate increased compared with that of the 0.1 slurry; this behavior could be attributed to the rod-like shape of the Fe_2O_3 nanoparticles. At the lower $\dot{\gamma}$, the particles were randomly oriented and the measured viscosity was high, whereas, as the $\dot{\gamma}$ increased, the

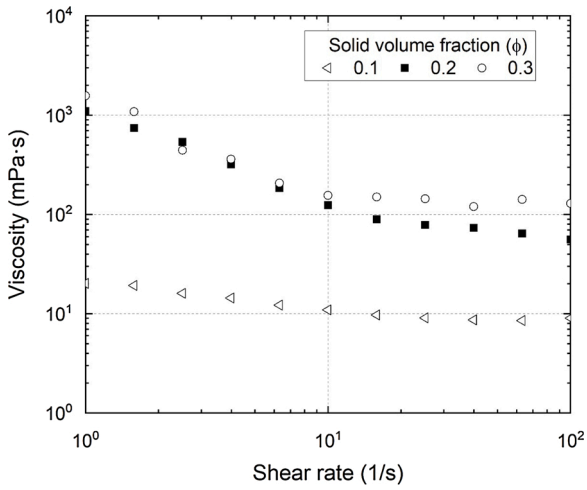

Fig. 1. Viscosity of Fe_2O_3 nanoparticles/camphene suspensions with different solid volume fractions (ϕ).

particles were aligned to the flow direction and the viscosity decreased. This situation became more relevant as the volume fraction of the solid increased. This shear-thinning behavior could be fitted with the Sisko model in accordance with Eq. 1 [31]:

$$\eta = \eta_{\infty} + K \cdot \dot{\gamma}^{(n-1)} \quad (1)$$

Where η_{∞} represents the viscosity when $\dot{\gamma} \to \infty$, K is the consistency parameter, and n is the flow index. This model was selected between many others available in the literature because its use is recommended for systems exhibiting infinite shear rate viscosity (η_{∞}).

The rheological parameters (Table 1) of the Fe_2O_3 nanoparticles/camphene suspensions according to the ϕ with the Sisko model were calculated using η_{100} as η_{∞}, since nearly constant viscosity was achieved in all measurements in that shear rate. As the ϕ increases, the n value in the flow index falls from 0.25 for $\phi = 0.1$ down to zero at $\phi = 0.2$ and 0.3. When $n = 0$, it agrees with a complete shear-thinning behavior, which transforms the Sisko model to a power law expression (i.e., Ostwald model) with the inclusion of the η_{∞} factor, by showing the effect of the shear stress and the particle alignment with the flow direction.

In fact, the particle alignment could be intensified by the effect of the SA as dispersant agent. The SA is a fatty acid with an 18-carbon chain molecule with a carboxyl functional group at one of its ends and molecular weight of 284.48 g·mol^{-1} (almost 5 times lower than the molecular weight of Hypermer KD4®, 1414.35 g·mol^{-1} [27]). The functional group forms a strong anchoring bond via ionic interaction with the hematite particle surface, the SA layer formed reduces the particle attraction forces and produces low viscosity Fe_2O_3 nanoparticles/camphene suspensions by steric hindrance. This effects have been reported previously for NiO nanoparticles suspensions [32] and calcium sulfate whisker [33] with SA as dispersant agent. Then, the adsorbed layer of SA is about 2 nm, and keep the particles apart around another 4 nm, these distances are within the order of magnitude of the rod-like shape Fe_2O_3 nanoparticles used, therefore, the particle alignment is not hinder by the SA molecules as the shear stress increased during viscosity measurements.

Table 1
Rheological parameters (consistency (K), flow index ($n - 1$), viscosity at 100 s^{-1} (η_{100}), as well as η_{∞}) of the Fe_2O_3 nanoparticles/camphene suspensions according to the solid volume fraction (ϕ) with the Sisko model [Eq. (1)].

ϕ	K (mPa·s^n)	$n - 1$	η_{100} (mPa·s)	η_{∞} (mPa·s)
0.1	13	−0.75	9	7
0.2	1062	−1.00	61	29
0.3	1352	−1.00	130	97

Fig. 2 shows the effect of the SA dispersant concentration over η_{100}. At 1 wt.% SA, the measured η_{100} was 142 mPa·s; as the concentration increased, the viscosity decreased continuously down to a minimal viscosity of 2.5 mPa·s with SA set at 4 wt.%. Furthermore, an increase in SA concentration produced a viscosity increment of up to 9 mPa·s. Therefore, the initial 8 wt.% could be considered to be above the optimal concentration of the dispersant agent, since several studies have determined an optimal dispersant concentration around the minimum viscosity value [27,34,35]. Lu et al. [29] verified how the minimal viscosity value moves towards a higher concentration of dispersant when the load of solid particles increases. Thus, as the dispersant concentration was kept constant for the different values of ϕ studied, the 8 wt.% dispersant concentration may be closer to the optimal dispersant concentration for $\phi = 0.3$. Table 2 shows the porosity measurements and the pore features of the Fe_2O_3 scaffolds according to the solid volume fraction (ϕ); the wall density of samples with $\phi = 0.1$ and 0.2 was significantly low due to the poor packing of the particles during solidification. Since 8 wt.% SA lies above the optimal concentration, the particles were completely surrounded by the dispersant, while the excess dispersant remained suspended in the solvent, which caused an increase in the values of η_{100}. The excess dispersant isolates the particles and hinders their adhesion during the solidification process, which prevents them from packing efficiently [36,37]. As ϕ approached 0.2, the wall density increased, since particles approached the optimal dispersant concentration. At $\phi = 0.3$, the wall density increased significantly (Table 2) due to a better particle packing during camphene solidification. It is possible that the surface of the particles was not completely covered because the optimal dispersant concentration could have been unattained, which allowed the decrease of micro-porosities in the walls, since the particles were packed closely due to the dominance of the van der Waals forces [35]. Open and close porosity were obtained by the Archimedes' method where the maximum porosity combined should equal to the volume fraction of camphene used to fabricate each Fe_2O_3 scaffolds. During freeze-casting, the camphene dendrites grows within a more stable particle suspension, where Fe_2O_3 nanoparticle sedimentation have been reduced by the use of SA, as no significant differences among the total porosity were observed across the sample height. Also, the dendrite replication was improved due to the lower effective particle size promoted by the short tail length of the SA molecule, this feature allows the primary/secondary arms to grow and produces a higher interconnected pore structure, even with an high particle loading, i.e. $\phi = 0.3$. This pore interconnectivity would allow the gas streams of reductant and oxidizing gases to flow alternatively throughout the scaffold and carry out the redox cycles. Clearly, lower ϕ will produces sample with higher open porosity but

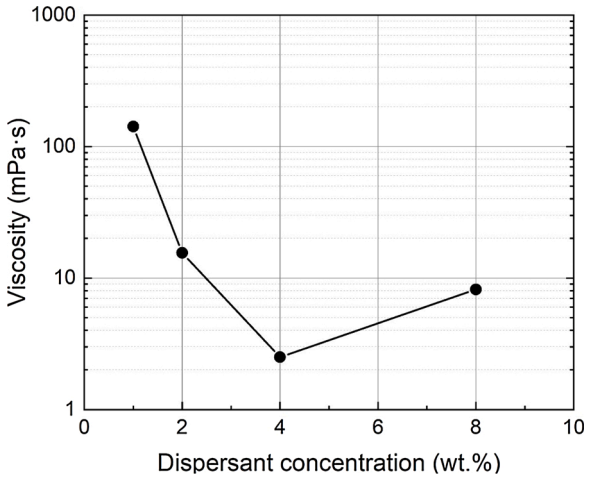

Fig. 2. Influence of the stearic acid dispersant concentration on the viscosity (η_{100}) of Fe_2O_3 nanoparticles/camphene suspensions with 0.1 solid volume fraction (ϕ).

Table 2
Porosity measurements and microstructural features of the Fe_2O_3 scaffolds according to the solid volume fraction (ϕ) using 8 wt.% of SA.

ϕ	Archimedes' method			Mercury Porosimetry		Optical Microscopy			
	Wall density (g/cm^3)	Open/close porosity (%)	Total porosity (%)	Bulk density (g/cm^3)	Total Porosity (%)	*h* (mm)	Total porosity (%)	Pore size (μm)	Wall thickness (μm)
0.1	1.51	66.3/4.8	71.1	1.31	75.0	9	74.7	103 ± 65	17 ± 8
						6	74.8	105 ± 65	15 ± 7
						3	74.6	103 ± 62	16 ± 8
						0	75.4	54 ± 31	12 ± 6
0.2	2.51	48.1/4.0	52.1	2.20	57.9	9	65.3	58 ± 38	16 ± 7
						6	67.5	70 ± 32	17 ± 7
						3	67.9	42 ± 36	14 ± 6
						0	60.0	30 ± 21	13 ± 6
0.3	3.53	24.2/8.4	32.6	3.71	29.4	9	27.2	33 ± 15	30 ± 12
						6	25.1	35 ± 16	28 ± 13
						3	26.0	34 ± 16	31 ± 14
						0	23.1	32 ± 15	31 ± 14

minor mechanical properties, however this drawback might be reduced with an improvement in the particle stacking within the scaffold walls.

3.2. Pore morphology and microstructure

Fig. 3 shows the effects of the directional solidification and the solid volume fraction over the final scaffold microstructure, where the FESEM micrographs analysis shows a decrease in porosity and pore size with the solid load (Table 2). The use of axial directional cooling to fabricate the Fe_2O_3 scaffolds produced a variation in the thermal gradient and in the solidification rate along the sample height [13]. This situation led the pore size to increase with no significant differences in the total porosity, although this gradient was attenuated with the increase of ϕ. Due to the combination of: 1) the SA as dispersant, 2) the pre-resting process and, 3) the cooling condition, no dense layer at the bottom of the samples was observed (Fig. 3a). The particle sedimentation was reduced and, the Fe_2O_3 nanoparticles/camphene suspensions encounter a lower thermal gradient at the beginning of the solidification.

Regarding pore morphology, the samples with ϕ = 0.1 tended to be elongated due to the dendritic growth of the camphene crystal with the primary arm oriented parallel to the direction of solidification (Fig. 3b), the small and equiaxed pores were created by the secondary arm oriented perpendicular. However, due to the increment of the solidification temperature with ϕ, the thermal gradient decreased, and the solidification front velocity increased during the progression of the front across the sample height. Thus, the tendency to form dendrites decreased and

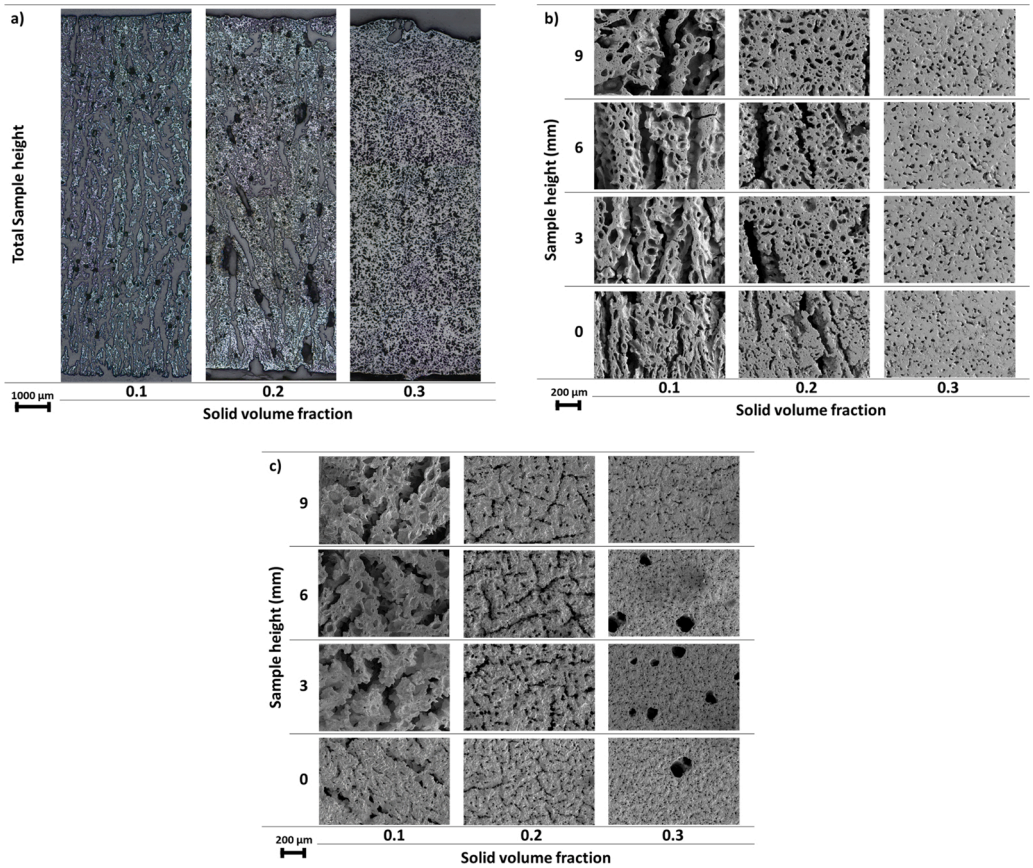

Fig. 3. Effect of the solid volume fraction (ϕ) on the pore morphology through the sample height: OM images of the overall morphology of the longitudinal section (a), FESEM images of the longitudinal (b), and cross-sections (c). FESEM micrographs were taken using the same magnification (200x) and the scale bar placed at the bottom left represents 200 μm.

the pore became equiaxed. This behavior was especially observed in samples with $\phi = 0.2$ (top part) and 0.3. FESEM micrographs of the cross-section (Fig. 3c) shows significant pore connectivity on samples with $\phi = 0.1$ and 0.2 throughout the height due to a dendrite coalescence during camphene solidification. Samples with $\phi = 0.3$ present scattered pores about 150 μm –most likely- due to some trapped air.

Table 2 shows the porosity values of the Fe_2O_3 scaffolds in terms of measurement techniques and ϕ. The total porosity of the samples decreased with the increment of ϕ, with a major reduction at $\phi = 0.3$ due to the volume contraction during sintering. The Archimedes' method and the Mercury Porosimetry measurements were similar in all ϕ as they calculated the open porosity of the samples by an intruded procedure. The optical measurements differed from those, most likely due to the extrapolation of 2D data to a volume magnitude and the lack of resolution of the small pores within the solid walls, which was particularly noticeable in the samples with the highest loading of close porosity. The close porosity increased significantly at $\phi = 0.3$ due to the particle entrapment promoted by the enhancement of the solidification rate and the increment of the solid concentration [38,39].

Table 2 also shows the average values of the pore size and wall thickness. Samples with $\phi = 0.1$ and 0.2 showed a gradient behavior throughout the sample height, with the smaller values being located at the bottom of the samples, where the highest cooling rate occurred. Due to the quantification method, the elongated pores were counted in terms of their thickness rather than their height, thus lowering the average pore size reported; however, a significant number of pores were round-shaped and were located within the solid walls. Gradient porosity is commonly observed in directional solidification samples [40], which is attributed to the variation of the thermal gradient and the camphene growth rate as the solid-liquid interfaces move across the sample. In the case of $\phi = 0.2$, a slight decrease in the average pore size was observed at the top of the sample (12 mm in height), probably caused by the increase in the local particle concentration due to the evaporation of camphene [41]. The gradient of the microstructure features decreased with the solid loading, since it was practically neglected at $\phi = 0.3$. At high solid loading, the local increment in particle concentration due to the pushing of the growing crystal, increasing the effective particle radius and lowering the critical velocity for particle engulfment [42], therefore, solid particles are being entrapped or engulfed rather than pushed, and the camphene crystal bridged during solidification. Later, those bridged are responsible for the significant level of interconnected porosity (open pores) achieved. The pore size distribution calculated by mercury intrusion (Fig. 4) shows wide histograms with mean pore sizes of 57, 13, and 12 mm for ϕ of 0.1, 0.2, and 0.3, respectively. The mean pore size determined by this technique represents the mean pore throat of the porous structure, which was significantly smaller than the pore size determined by OM analysis. This effect is already described in the literature [43] and it was enhanced by the interconnected pore structure obtained in the sintered Fe_2O_3 scaffolds.

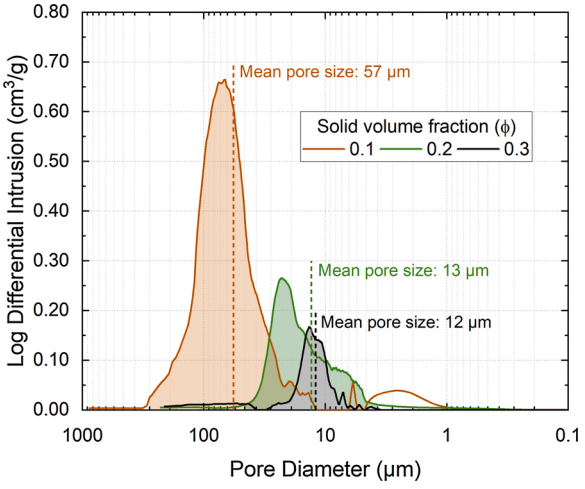

Fig. 4. Pore size distribution of the sintered Fe_2O_3 scaffolds for different solid volume fractions (ϕ). Mean pore size was calculated over the shaded area.

3.3. Effect of the solid volume fraction (ϕ) on viscosity

As was previously established, the interactions between particles in the liquid camphene caused an increase in the viscosity with the increase of ϕ. Despite the numerous correlations between the solid volume fraction (ϕ) and the apparent viscosity (η), the Krieger and Dougherty model [44] (Eq. 2) is commonly accepted for particles in camphene [19]:

$$\eta = \eta_{solvent} \cdot \left(1 - \frac{\phi}{\phi_{max}}\right)^{-[\eta]\cdot\phi_{max}} \quad (2)$$

Where $\eta_{solvent}$ is the viscosity of the solvent (1.60 mPa·s), φ_{max} is the maximum packing fraction, and $[\eta]$ represents the intrinsic viscosity. In this model, $[\eta]$ is a factor to describe the particle shape, which is typically reported as 2.5 for monodispersed hard spheres according to the Einstein relation. Since rod-like shaped nanoparticles were used in this study, a more suitable expression for low-aspect radio spheroids ($R < 15$) could be that as proposed by Zirnsak et al. [45] (Eq. 3):

$$[\eta] = 2.5 + 0.408\cdot(R-1)^{1.508} \quad (3)$$

$[\eta]$ could have values ranging from 4.64 for a nominal $R = 4$–11.89 for $R = 9$. This range provides a better understanding of how sensitive the slurries' viscosity could be to the morphological features of rod-like particles. Likewise, ϕ_{max} could be obtained from the critical solid volume fraction (ϕ_b), known as breakthrough [23], in which particles are no longer pushed by the growing camphene crystal, thereby forcing the solid/liquid interfaces to bypass (engulf) the packed particle, according to the following equation (Eq. 4):

$$\phi_{max} = \phi_b + \left(\frac{3KT}{32\pi\rho S_a \gamma (R_p)^3}\right)^{1/3} \quad (4)$$

where K is Boltzmann's constant, T is the solidification temperature, ρ is the hematite density (5.24 $g{\cdot}cm^{-3}$), S_a is the specific surface area, γ is the solid/liquid interfacial energy for the camphene (0.0044 $J{\cdot}m^{-2}$) [46], and R_p is the particle radius. Eq. 4 was adapted to cylindrical particles with a nominal $R = 4$. The ϕ_b value could be linearly extrapolated from the solid volume fraction of a zero-total porosity (i.e., fully dense) sample by the Archimedes' method as $\phi_b = 0.469$. Finally, the maximum packing fraction ϕ_{max} was estimated to be 0.569.

The solid volume fraction (ϕ) is affected by the SA adsorption layer (δ) bonded to the solid particles, which, assuming the deprotonated molecule length in a perpendicular disposition, is approximately 2.4 nm. Thus, an effective solid volume fraction (ϕ_{eff}) was calculated by modifying the Krieger-Dougherty equation [44] to consider rod-like particles, as follows (Eq. 5):

$$\phi_{eff} = \phi\left(1 - \frac{2\delta\rho S_a}{9}\right)^3 \quad (5)$$

Eq. 3 can be rewritten as:

$$\eta_\infty = \eta_{camphene} \cdot \left(1 - \frac{\phi_{eff}}{\phi_{max}}\right)^{-[\eta]\cdot\phi_{max}} \quad (6)$$

Fig. 5 shows the influence of the solid volume fraction of Fe_2O_3 nanoparticles/camphene suspensions with 8 wt.% of stearic acid on the viscosity. Initially, the increment of η_∞ observed with the ϕ follows the Krieger-Dougherty model, although the influences of the particle-aspect ratio is visible as $[\eta]$ resulted in 33. Fe_2O_3 particles had a nominal $R = 4$. However, the slurries seemed to follow a trend described by particles

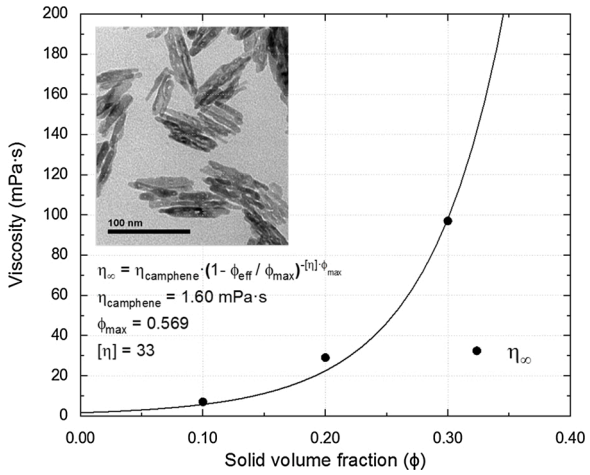

Fig. 5. Viscosity vs. volume fraction of Fe_2O_3 nanoparticles/camphene suspensions dispersed with 8 wt.% of stearic acid based on the Krieger-Dougherty model (Eq. 6). The TEM image inserted shows the rod-like shape of the nanoparticles used.

with a much higher aspect ratio, which could be the case since the nanoparticles with rod-like shapes usually align when a shear rate is applied. An $R = 18.5$ could be obtained using Eq. 3, but it is only suitable for spheroids with $R < 15$, however, Kuhn and Kuhn [47] proposed for high-aspect-ratio spheroids ($R >> 1$) a more complex expression which leads to a $R = 21$, a more appropriated value. Nevertheless, the theoretical viscosity of the slurries, used in the Krieger-Dougherty model of the slurries, could be underestimated, since the influence of the non-absorbed SA molecules that remained dissolved in the camphene was not considered. This situation was observed especially at ϕ =0.1, in which the optimal dispersant concentration was established at 4 wt.% (Fig. 2). Undoubtedly, the influence of the non-absorbed dispersant decreased with the further increase of the ϕ in the slurry.

3.4. Mechanical properties

Fig. 6 shows the stress-strain curves of the Fe_2O_3 scaffolds developed in this study according to their solid volume fraction (ϕ), height (h), and loading direction. Overall, all the curves showed a stepped evolution during the tests, since parts of the samples were scraped off during compression, especially at ϕ = 0.1 and 0.2; at the end of the test samples were unrecovered as their crumbled into coarse/finer particles. The compressive strength (σ) was obtained using the maximum strength reported on each test before rupture or an abrupt decrease of the applied stress. In general, σ and strain (%) were enhanced by the increase of solid load and when the samples were loaded parallel to the solidification direction. This is due to the influence of a more robust structure with a lower impact of defects, such as cracks, or to inefficient particle stacking during solidification. These defects were observed on samples with ϕ = 0.1 and 0.2 (Fig. 3).

Table 3 shows the average compressive strength obtained from the stress-strain curves of Fig. 6 In general terms, the samples tested at h = 0 showed a higher compressive strength than those at h = 9. This behavior is attributed to the increase in pore size observed with h, such different was reduced on samples tested perpendicular to the freezing direction and with the increases of ϕ. Fig. 7 shows a correlation of the compressive strength and the structural features, pore and wall size, with the solid volume fraction. The mechanical resistance increased when: 1) the pore size decreased, since porosity decreased with the increase of solid load; 2) the sample was measured at the bottom, where h = 0, the cooling rate was higher, and the solidification progress decreased; 3) the samples were loaded parallel to the cooling direction. The pore size reduction caused by the increase of solid load, seems to be linked to the mechanical performance, rather than to the wall densification achieved.

Furthermore, the samples with ϕ = 0.1 showed the lowest strength due to the low wall density achieved, although at h = 0, an average of 2.6 MPa was reported when stress was applied parallel to the solidification direction. When the sample was tested in the top part, the ratio of compressive strength (δ), taken as the parallel/perpendicular, was decrease. This is related to the presence of defects in the solid walls due to the poor packing of the particles during solidification, since SA in ϕ = 0.1 lies above the optimal concentration, which counterbalances the pore morphology structural aspects, thereby making the mechanical behavior more isotropic. The average compressive strength increased in samples with ϕ = 0.2, whereby the increase of solid load and the decrease of pore size presented the principal reasons. In this sample, δ increased to 1.7 and 1.4 at h = 0 and h = 9, respectively. This behavior indicates that the scaffold structure is less dependent on the presence of defects and is more influenced by the pore morphology. Surprisingly, δ values were lower than those reported in the literature for ceramic materials fabricated by freeze-casting [48–50]; this could be caused by the highly interconnected pore structure created by the solidification of

Table 3
Average compressive strength σ of the Fe_2O_3 scaffolds according to the solid volume fraction (ϕ), height (h) and loading direction.

ϕ	h (mm)	Compressive strength (MPa)		
		Parallel	Perpendicular	δ
0.1	9	1.7 ± 0.5	1.7 ± 0.2	1.0
	0	2.6·± 0.7	1.5 ± 0.3	1.7
0.2	9	6.3 ± 0.1	4.5 ± 0.2	1.4
	0	7.5 ± 0.1	4.4 ± 0.8	1.7
0.3	9	77.3 ± 3.5	73.0 ± 0.5	1.1
	0	106.9 ± 12.5	90.0 ± 7.1	1.2

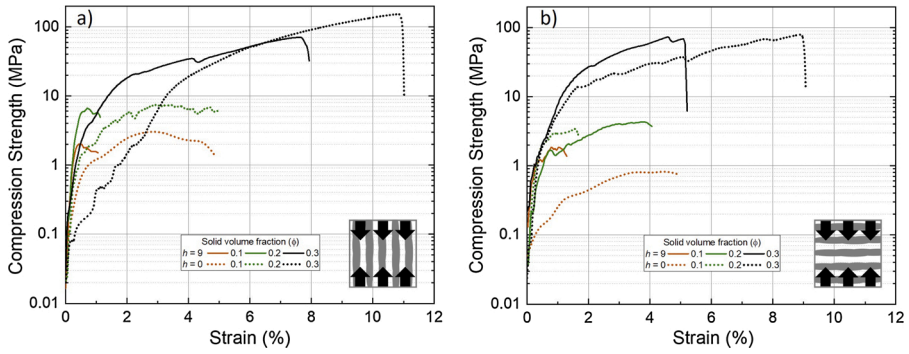

Fig. 6. Stress–strain curves of the sintered Fe_2O_3 scaffolds for different solid volume fractions (ϕ) and loading directions. Samples were loaded parallel (a) or perpendicular (b) to the direction of solidification at final h = 9 and h = 0.

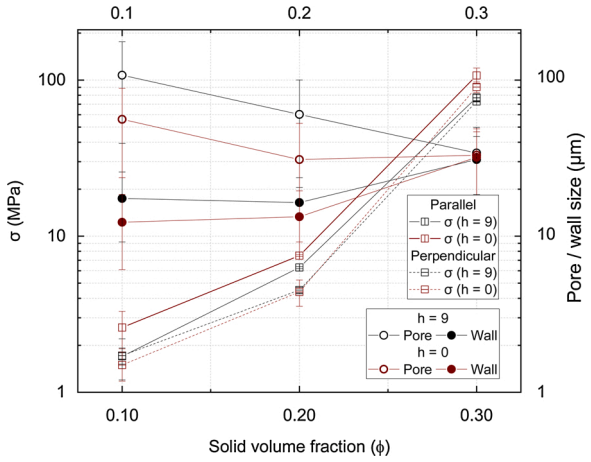

Fig. 7. Compressive strength (σ), pore and wall size of the sintered Fe_2O_3 scaffolds for different solid volume fractions (ϕ), loading directions, and sample positions (*h*). The error bars represent the standard deviation of each measurement.

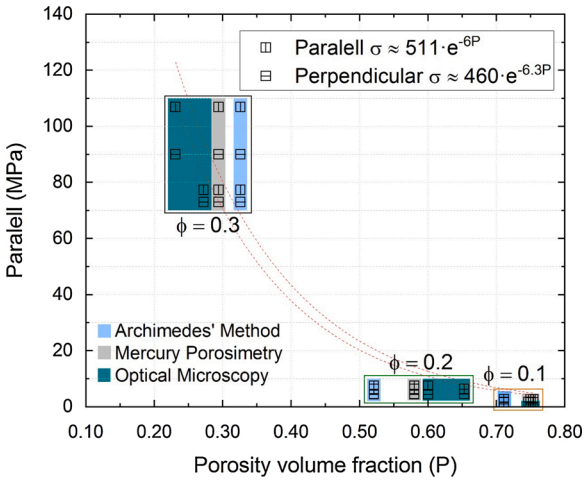

Fig. 8. Evolution of the compressive strength vs. the porosity volume fraction (*P*). *P* is the total porosity obtained by Archimedes' Method, Mercury Porosimetry and Optical Microscopy (Table 2).

a highly branched camphene crystal [51], which is enhanced by the use of SA, since it lowers the viscosity and favors solid front mobility. The samples with ϕ = 0.3 showed the highest compressive strength, with a noticeable increase at the bottom of the sample due to a reduction in porosity, however, no significant variation on the compressive strength was observed according to the loading direction. As is shown in Fig. 3, no directional porosity was created when the solid loading increased up to 0.3, and the scaffold pore structure became isotropic.

Fig. 8 shows the increase of the compression resistance with the decrease of the measured porosity, as the samples were tested either parallel or perpendicular to the solidification direction. This behavior could be fitted within the minimum solid area model proposed by Rice [52], where a mechanical property varies according to the following equation (Eq. 7):

$$\sigma = \sigma_{solid} \cdot e^{-b \cdot P} \quad (7)$$

Where σ is the average compression strength measured, σ_{solid} is the compression strength of the fully-dense Fe_2O_3, P is the porosity volume fraction, and b is the pore geometry factor. The minimum solid area model is based on the effect of the pore shape on the loading bearing area (i.e., minimum solid bond), where b may have 1.4–3 for cylindrical or spherical pores in cubic stacking, or 5–9 for solid spheres in cubic or rhombohedral stacking, respectively. In this work, the model indicates b values of 6 and 6.3 for the σ parallel and perpendicular loading directions, respectively, which suggests that the material structure fits better with a solid/particle stacking arrangement rather than an elongated-alignment porosity. This behavior is due to the effects of the excess of SA interfering with the particle packing during solidification on samples with ϕ = 0.1 and 0.2, which lowers the solid contacts even after sintering. This effect produces a similar mechanical behavior since the loading was performed parallel or perpendicular. There is a noticeable uncertainty in the previous fitting, since no suitable data was found for σ_{solid} ; however, fitting curves (inserted in Fig. 8) show a fully-dense Fe_2O_3 sample with a parallel and perpendicular compression strength of 511 ± 75 MPa and 460 ± 65 MPa, respectively. These values are similar and comparable (within the same order of magnitude) to those of other oxide ceramic materials [50,53–55].

4. Conclusion

Stearic acid showed a prominent capacity to reduce the apparent viscosity (η) of camphene-based suspension with a high solid volume fraction (ϕ) of nanometric particles. The viscosity (η_∞) of this suspension follows the Krieger and Dougerty model, although the particle shape modifies the rheological behavior according to the effective solid volume fraction (ϕ_{eff}) described in this study.

The samples, prepared by freeze-casting using SA as the dispersant agent, showed a significant decrease in the porosity gradient with a low ratio of compressive strength (δ). The Fe_2O_3 scaffolds over 70 % of total porosity were successfully fabricated with notable compressive strength. The mechanical performance of the Fe_2O_3 scaffolds improved with the increase in the solid volume fraction (ϕ), and showed a compressive strength of 106.9 MPa loading parallel to the solidification direction.

The use of the SA as the dispersant agent improved the rheological behavior of Fe_2O_3 nanoparticle slurries by lowering the viscosity and improving the particle stacking during freeze-casting. Therefore, Fe_2O_3 scaffolds may be fabricated with higher porosity levels with no significant repercussions in mechanical performance, while the number of structural defects in the solid walls may be reduced. This leads to an improvement in the redox performance since the sintering process in the scaffolds will be delayed or prevented.

Data availability

The raw data required to reproduce these findings are available to download from http://www.inciemat.es/.

Declaration of Competing Interest

The authors declare that they have no known competing financial interests or personal relationships that could have appeared to influence the work reported in this paper.

Acknowledgements

Financial support for this work has been provided by the Ministerio de Ciencia e Innovación – Agencia Estatal de Investigación through the project MAT2016-76713-P co-funded by European Regional Development Fund. Lloreda-Jurado P.J. also thanks the University of Seville for its financial support (grant PIF II.2A, through VI Plan Propio de Investigación). The authors are also grateful for the postdoctoral contract of Víctor Pérez Puyana (PAIDI-DOCTOR, Junta de Andalucía – Universidad de Sevilla).

References

[1] W.L. Li, K. Lu, J.Y. Walz, Freeze casting of porous materials: review of critical factors in microstructure evolution, Int. Mater. Rev. 57 (2012) 37–60, https://doi.org/10.1179/1743280411Y.0000000011.

[2] S. Deville, Ice-templating, freeze casting: beyond materials processing, J. Mater. Res. 28 (2013) 2202–2219, https://doi.org/10.1557/jmr.2013.105.

[3] T. Ilzig, D. Schumacher, M. Wilhelm, S. Günther, S. Odenbach, Image data analysis of high resolution μCT data for the characterization of pore orientation and pore space interconnectivity in freeze cast ceramics, Mater. Charact. 174 (2021) 110966, https://doi.org/10.1016/j.matchar.2021.110966.

[4] D.F. Souza, E.H.M.M. Nunes, D.S. Pimenta, D.C.L.L. Vasconcelos, J.F. Nascimento, W. Grava, M. Houmard, W.L. Vasconcelos, Synthesis and structural evaluation of freeze-cast porous alumina, Mater. Charact. 96 (2014) 183–195, https://doi.org/10.1016/j.matchar.2014.08.009.

[5] S.W. Sofie, F. Dogan, Freeze casting of aqueous alumina slurries with glycerol, J. Am. Ceram. Soc. 84 (2001) 1459–1464, https://doi.org/10.1111/j.1151-2916.2001.tb00860.x.

[6] T. Fukasawa, M. Ando, T. Ohji, S. Kanzaki, Synthesis of porous ceramics with complex pore structure by freeze-dry processing, J. Am. Ceram. Soc. 84 (2001) 230–232, https://doi.org/10.1111/j.1151-2916.2001.tb00638.x.

[7] T. Waschkies, R. Oberacker, M.J. Hoffmann, Control of lamellae spacing during freeze casting of ceramics using double-side cooling as a novel processing route, J. Am. Ceram. Soc. 92 (2009) S79–S84, https://doi.org/10.1111/j.1551-2916.2008.02673.x.

[8] S.M. Miller, X. Xiao, K.T. Faber, Freeze-cast alumina pore networks: effects of freezing conditions and dispersion medium, J. Eur. Ceram. Soc. 35 (2015) 3595–3605, https://doi.org/10.1016/j.jeurceramsoc.2015.05.012.

[9] Y. Lin, J. Chen, S. Dong, G. Wu, P. Jiang, X. Huang, Wet-resilient graphene aerogel for thermal conductivity enhancement in polymer nanocomposites, J. Mater. Sci. Technol. 83 (2021) 219–227, https://doi.org/10.1016/j.jmst.2020.12.051.

[10] L. Yan, J. Wu, L. Zhang, X. Liu, K. Zhou, B. Su, Pore structures and mechanical properties of porous titanium scaffolds by bidirectional freeze casting, Mater. Sci. Eng. C. 75 (2017) 335–340, https://doi.org/10.1016/j.msec.2016.12.044.

[11] S.-W. Yook, H.-D. Jung, C.-H. Park, K.-H. Shin, Y.-H. Koh, Y. Estrin, H.-E. Kim, Reverse freeze casting: a new method for fabricating highly porous titanium scaffolds with aligned large pores, Acta Biomater. 8 (2012) 2401–2410, https://doi.org/10.1016/j.actbio.2012.03.020.

[12] D. Schumacher, D. Zimnik, M. Wilhelm, M. Dreyer, K. Rezwan, Solution based freeze cast polymer derived ceramics for isothermal wicking - relationship between pore structure and imbibition, Sci. Technol. Adv. Mater. 20 (2019) 1207–1221, https://doi.org/10.1080/14686996.2019.1699766.

[13] P.J. Lloreda-Jurado, E.M. Pérez-Soriano, A. Paúl, J. Herguido, J.A. Peña, R. Sepúlveda, Doped iron oxide scaffolds with gradient porosity fabricated by freeze casting: pore morphology prediction and processing parameters, Mater. Sci. Technol. 36 (2020) 1227–1237, https://doi.org/10.1080/02670836.2020.1765096.

[14] H. Park, H.H. Cho, K. Kim, K. Hong, J.H. Kim, H. Choe, D.C. Dunand, Surface-oxidized, freeze-cast cobalt foams: microstructure, mechanical properties and electrochemical performance, Acta Mater. 142 (2018) 213–225, https://doi.org/10.1016/j.actamat.2017.09.066.

[15] G. Voitic, V. Hacker, Recent advancements in chemical looping water splitting for the production of hydrogen, RSC Adv. 6 (2016) 98267–98296, https://doi.org/10.1039/C6RA21180A.

[16] Y. Saito, F. Kosaka, N. Kikuchi, H. Hatano, J. Otomo, Evaluation of microstructural changes and performance degradation in iron-based oxygen carriers during redox cycling for chemical looping systems with image analysis, Ind. Eng. Chem. Res. 57 (2018) 5529–5538, https://doi.org/10.1021/acs.iecr.7b04966.

[17] S.K. Wilke, D.C. Dunand, Structural evolution of directionally freeze-cast iron foams during oxidation/reduction cycles, Acta Mater. 162 (2019) 90–102, https://doi.org/10.1016/j.actamat.2018.09.054.

[18] P.J. Lloreda-Jurado, J. Hernández-Saz, E. Chicardi, A. Paúl, R. Sepúlveda, Pore morphology evolution and atom distribution of doped Fe_2O_3 foams developed by freeze-casting after redox cycling, J. Mater. Res. Technol. 13 (2021) 1887–1898, https://doi.org/10.1016/j.jmrt.2021.06.008.

[19] K. Araki, J.W.J.W. Halloran, New freeze-casting technique for ceramics with sublimable vehicles, J. Am. Ceram. Soc. 87 (2004) 1859–1863, https://doi.org/10.1111/j.1151-2916.2004.tb06331.x.

[20] H.A. Smith, J.F. Fuzek, H.T. Meriwether, The catalytic hydrogenation of terpenes, J. Am. Chem. Soc. 71 (1949) 3765–3769, https://doi.org/10.1021/ja01179a054.

[21] E.R.R. Rubinstein, M.E.E. Glicksman, Dendritic growth kinetics and structure II. Camphene, J. Cryst. Growth 112 (1991) 97–110, https://doi.org/10.1016/0022-0248(91)90915-R.

[22] Y.-H. Koh, E.-J. Lee, B.-H. Yoon, J.-H. Song, H.-E. Kim, H.-W. Kim, Effect of Polystyrene Addition on Freeze Casting of Ceramic/Camphene Slurry for Ultra-High Porosity Ceramics with Aligned Pore Channels, J. Am. Ceram. Soc. 89 (2006) 3646–3653, https://doi.org/10.1111/j.1551-2916.2006.01311.x.

[23] N.O. Shanti, K. Araki, J.W. Halloran, Particle redistribution during dendritic solidification of particle suspensions, J. Am. Ceram. Soc. 89 (2006) 2444–2447, https://doi.org/10.1111/j.1551-2916.2006.01094.x.

[24] Y.-W. Moon, K.-H. Shin, Y.-H. Koh, W.-Y. Choi, H.-E. Kim, Porous alumina ceramics with highly aligned pores by heat-treating extruded alumina/camphene body at temperature near its solidification point, J. Eur. Ceram. Soc. 32 (2012) 1029–1034, https://doi.org/10.1016/J.JEURCERAMSOC.2011.11.035.

[25] M.K. Ahn, Y.W. Moon, W.Y. Maeng, Y.H. Koh, H.E. Kim, Calcium phosphate ceramics with continuously gradient macrochannels using three-dimensional extrusion of bilayered ceramic-camphene mixture/pure camphene feedrod, Ceram. Int. 42 (2016) 15603–15609, https://doi.org/10.1016/j.ceramint.2016.07.013.

[26] V.M.B. Moloney, D. Parris, M.J. Edirisinghe, Rheology of zirconia suspensions in a nonpolar organic medium, J. Am. Ceram. Soc. 78 (1995) 3225–3232, https://doi.org/10.1111/j.1151-2916.1995.tb07958.x.

[27] S. Zürcher, T. Graule, Influence of Dispersant Structure on the Rheological Properties of Highly-concentrated Zirconia Dispersions, 25, 2005, pp. 863–873, https://doi.org/10.1016/j.jeurceramsoc.2004.05.002.

[28] T. Hildebrand, P. Rüegsegger, A new method for the model-independent assessment of thickness in three-dimensional images, J. Microsc. 185 (1997) 67–75, https://doi.org/10.1046/j.1365-2818.1997.1340694.x.

[29] K. Lu, C.S. Kessler, R.M. Davis, Optimization of a nanoparticle suspension for freeze casting, J. Am. Ceram. Soc. 89 (2006) 2459–2465, https://doi.org/10.1111/j.1551-2916.2006.01111.x.

[30] M. Felix, V. Perez-Puyana, A. Paúl, R. Sepúlveda, Camphene/polystyrene solutions: a rheological approach for material processing industry, J. Appl. Polym. Sci. 136 (2019), https://doi.org/10.1002/app.47953.

[31] A.W. Sisko, The flow of lubricating greases, Ind. Eng. Chem. 50 (1958) 1789–1792, https://doi.org/10.1021/ie50588a042.

[32] P.J. Lloreda-Jurado, E. Chicardi, A. Paúl, R. Sepúlveda, Effect of processing parameters on the properties of freeze-cast Ni wick with gradient porosity, Mater. Des. 206 (2021) 109795, https://doi.org/10.1016/j.matdes.2021.109795.

[33] W. Yuan, J. Cui, S. Xu, Mechanical properties and interfacial interaction of modified calcium sulfate Whisker/Poly(Vinyl chloride) composites, J. Mater. Sci. Technol. 32 (2016) 1352–1360, https://doi.org/10.1016/j.jmst.2016.05.016.

[34] K. Lu, Æ.C. Kessler, Colloidal Dispersion and Rheology Study of Nanoparticles, 2006, pp. 5613–5618, https://doi.org/10.1007/s10853-006-0303-5.

[35] J. Zou, Y. Zhang, R. Li, Effect of suspension state on the pore structure of freeze-cast ceramics, Int. J. Appl. Ceram. Technol. 8 (2011) 482–489, https://doi.org/10.1111/j.1744-7402.2009.02458.x.

[36] K. Lu, Microstructural evolution of nanoparticle aqueous colloidal suspensions during freeze casting, J. Am. Ceram. Soc. 90 (2007) 3753–3758, https://doi.org/10.1111/j.1551-2916.2007.02000.x.

[37] A.U. Khan, N. Mahmood, P.F. Luckham, Rheological characterization of alumina ceramic suspensions in presence of a dispersant and a binder, J. Dispers. Sci. Technol. 33 (2012) 1210–1217, https://doi.org/10.1080/01932691.2011.605646.

[38] S.T. Oh, S.Y. Chang, M.J. Suk, Microstructure of porous Cu fabricated by freeze-drying process of CuO/camphene slurry, Trans. Nonferrous Met. Soc. China (English Ed. 22 (2012) s688–s691, https://doi.org/10.1016/S1003-6326(12)61787-7.

[39] R. Liu, T. Xu, C. Wang, A review of fabrication strategies and applications of porous ceramics prepared by freeze-casting method, Ceram. Int. 42 (2016) 2907–2925, https://doi.org/10.1016/j.ceramint.2015.10.148.

[40] C. Hong, J. Du, J. Liang, X. Zhang, J. Han, Functionally graded porous ceramics with dense surface layer produced by freeze-casting, Ceram. Int. 37 (2011) 3717–3722, https://doi.org/10.1016/j.ceramint.2011.04.119.

[41] J. Du, X. Zhang, C. Hong, W. Han, Microstructure and mechanical properties of ZrB2–SiC porous ceramic by camphene-based freeze casting, Ceram. Int. 39 (2013) 953–957, https://doi.org/10.1016/j.ceramint.2012.07.012.

[42] S. Sen, W.F. Kaukler, P. Curreri, D.M. Stefanescu, Dynamics of solid/liquid interface shape evolution near an insoluble particle - an X-ray transmission microscopy investigation, Metall. Mater. Trans. A Phys. Metall. Mater. Sci. 28 (1997) 2129–2135, https://doi.org/10.1007/s11661-997-0170-y.

[43] H. Giesche, Mercury porosimetry: a general (Practical) overview, Part. Part. Syst. Charact. 23 (2006) 9–19, https://doi.org/10.1002/ppsc.200601009.

[44] I.M. Krieger, T.J. Dougherty, A mechanism for non-newtonian flow in suspensions of rigid spheres, Trans. Soc. Rheol. 3 (1959) 137–152, https://doi.org/10.1122/1.548848.

[45] M.A. Zirnsak, D.U. Hur, D.V. Boger, Normal stresses in fibre suspensions, J. Nonnewton, Fluid Mech. 54 (1994) 153–193, https://doi.org/10.1016/0377-0257(94)80020-0.

[46] B. Bayender, N. Maraşlı, E. Çadırlı, M. Gündüz, Solid–liquid interfacial energy of camphene, Mater. Sci. Eng. A. 270 (1999) 343–348, https://doi.org/10.1016/S0921-5093(99)00162-8.

[47] W. Kuhn, H. Kuhn, Die Abhängigkeit Der Viskosität Vom Strömungsgefälle bei hochverdünnten suspensionen und Lösungen, Helv. Chim. Acta 28 (1945) 97–127, https://doi.org/10.1002/hlca.19450280111.

[48] Y.-M. Soon, K.-H. Shin, Y.-H. Koh, J.-H. Lee, H.-E. Kim, Compressive strength and processing of camphene-based freeze cast calcium phosphate scaffolds with aligned pores, Mater. Lett. 63 (2009) 1548–1550, https://doi.org/10.1016/j.matlet.2009.04.013.

[49] Y.-M. Soon, K.-H. Shin, Y.-H. Koh, W.-Y. Choi, H.-E. Kim, Assembling unidirectionally frozen alumina/camphene bodies for aligned porous alumina ceramics with larger dimensions, J. Eur. Ceram. Soc. 31 (2011) 415–419, https://doi.org/10.1016/j.jeurceramsoc.2010.09.019.

[50] J. Han, C. Hong, X. Zhang, J. Du, W. Zhang, Highly porous ZrO2 ceramics fabricated by a camphene-based freeze-casting route: microstructure and properties, J. Eur. Ceram. Soc. 30 (2010) 53–60, https://doi.org/10.1016/j.jeurceramsoc.2009.08.018.

[51] H. Park, T. Um, K. Hong, J.S. Kang, H.-S. Nam, K. Kwon, Y.-E. Sung, H. Choe, Effects of Powder Carrier on the Morphology and Compressive Strength of Iron Foams: Water vs Camphene, Metall. Mater. Trans. B. 49 (2018) 2182–2190, https://doi.org/10.1007/s11663-018-1302-z.

[52] R.W. Rice, Evaluation and extension of physical property-porosity models based on minimum solid area, J. Mater. Sci. 31 (1996) 102–118, https://doi.org/10.1007/BF00355133.

[53] J.-W. Moon, H.-J. Hwang, M. Awano, K. Maeda, Preparation of NiO–YSZ tubular support with radially aligned pore channels, Mater. Lett. 57 (2003) 1428–1434, https://doi.org/10.1016/S0167-577X(02)01002-9.
[54] C. Hong, X. Zhang, J. Han, J. Du, W. Zhang, Camphene-based freeze-cast ZrO2 foam with high compressive strength, Mater. Chem. Phys. 119 (2010) 359–362, https://doi.org/10.1016/j.matchemphys.2009.10.031.
[55] S.W. Yook, H.E. Kim, B.H. Yoon, Y.M. Soon, Y.H. Koh, Improvement of compressive strength of porous hydroxyapatite scaffolds by adding polystyrene to camphene-based slurries, Mater. Lett. 63 (2009) 955–958, https://doi.org/10.1016/j.matlet.2009.01.080.